Frontiers of Physics
https://doi.org/10.1007/s11467-022-1154-5
Front. Phys.
17(5), 53504 (2022)

RESEARCH ARTICLE

Novel two-dimensional PdSe phase: A puckered material with excellent electronic and optical properties

Mingyun Huang[1], Xingxing Jiang[1], Yueshao Zheng[1], Zhengwei Xu[1], Xiong-Xiong Xue[2,†], Keqiu Chen[1], Yexin Feng[1,‡]

[1] *Hunan Provincial Key Laboratory of Low-Dimensional Structural Physics & Devices, School of Physics and Electronics, Hunan University, Changsha 410082, China*
[2] *School of Physics and Optoelectronics, Xiangtan University, Xiangtan 411105, China*
Corresponding authors. E-mail: †xxxue@xtu.edu.cn, ‡yexinfeng@pku.edu.cn
Received November 13, 2021; accepted February 15, 2022

By combining structural search and first-principles calculations, we predict a new stable two-dimensional PdSe monolayer, and systematically investigate its structural, electronic and optical properties. The calculated formation enthalpy, phonon spectra and molecular dynamic simulations confirm that PdSe monolayer possesses excellent thermodynamic and dynamic stability. PdSe monolayer is a semiconductor with an indirect band gap of ∼ 1.10 eV. The carrier transport of PdSe monolayer is dominated by hole and exhibits remarkable anisotropy due to the intrinsic structure anisotropy. The optical properties also show obvious anisotropic characteristic with considerable absorption coefficient and broad absorption from the visible to ultraviolet regions. Benefiting from these excellent physical properties, PdSe monolayer is expected to be a promising candidate as electronic and optoelectronic devices.

Keywords first-principles calculation, two-dimensional (2D), electronic structure, structural search, PdSe

1 Introduction

Two-dimensional (2D) materials have attracted wide attention due to their unique structural and electronic properties, such as adjustable band gap, high carrier mobility and high transparency. These excellent properties provide significant opportunities for catalysis, energy conversion and optoelectronic devices [1–5]. Since the successful exfoliation of graphene [6–8], it has gained a lot of attention in physical, chemical and material fields because of high carrier mobility, superconductivity and high thermal conductivity [9–12]. Although graphene possesses many advantages, it is difficult to obtain a desirable band gap, which hinders its application in the field of optoelectronics. This challenge has motivated people to further explore many other 2D materials beyond graphene, such as hexagonal boron nitride (h-BN) [13, 14], transition metal dichalcogenides (TMDs) [15–18], phosphorene [19–21], Metal Organic Frameworks [22–24] and borophene [25, 26], etc.

For electronic and optoelectronic applications, a material with good air stability and appropriate band gap (small than 1.50 eV) is more desirable [27, 28]. Unfortunately, the band gaps of many obtained 2D semiconductors are larger than 1.5 eV, such as 4.50 eV for h-BN and 1.79 eV for MoS_2 monolayers. Therefore, searching new 2D semiconductors with a band gap in the range of 0.3–1.5 eV is very important for the development of new efficient electronic and optoelectronic devices.

In last few years, the compounds of Pd and Se elements have attracted attention of many researchers. Sun *et al.* [2] reported the band structure, transport and optical properties of monolayer and bulk $PdSe_2$ (per unit cell contains 2Pd and 4Se atoms) by first-principles calculations. Liang *et al.* [29] successfully synthesized a pentagonal layered $PdSe_2$, in which reversable defect states and the migrations of Se-vacancy defects with STM technique were observed. Lin *et al.* [30] demonstrated that a novel Pd_2Se_3 (per unit cell contains 4 Pd and 6 Se atoms) monolayer could be successfully synthesized by introducing Se vacancies in $PdSe_2$ bilayer. The Se vacancies of $PdSe_2$ bilayer reduced the distance between layers, assisting the melding of bilayer $PdSe_2$ into Pd_2Se_3 monolayer. Furthermore, Zhu *et al.* [31] revealed that Pd_2Se_3 possesses an appropriate band structure for electronic and optoelectronic applications. Considering these outstanding electronic properties of various 2D Pd–Se compounds, we believe that it is of great significance to systematically search new stable 2D Pd–Se structures with varying Pd:Se ratio.

In this paper, based on density functional theory (DFT)

* This article can also be found at http://journal.hep.com.cn/fop/EN/10.1007/s11467-022-1154-5.

calculations, we studied several 2D Pd_xSe_y (x, y =1–4) structures, which are generated by modifying reported Pd–Se structures, such as Pd_2Se_4 and Pd_4Se_6 (for better comparison, we named after the number of atoms per unit cell) and systematically studied their stability, structural, electronic and optical properties. Then, with the assist of an efficient structure searching method, we identified a novel puckered PdSe monolayer with the stoichiometric ratio of 1∶1. The formation enthalpy, phonon spectra and molecular dynamics simulation results clearly suggested that this PdSe monolayer is thermodynamical and dynamic stable. PdSe monolayer possesses an indirect band gap (1.10 eV) and the band structures of multilayers reveal obvious quantum confinement effect. PdSe monolayer also exhibits superb absorption coefficients and optical anisotropies in the visible region, which renders it as a desirable candidate in optoelectronic devices and polarized optical sensors.

2 Computational methods

The structure prediction for Pd_xSe_y monolayer is based on particle swarm optimization (PSO) method, which is applied in the Crystal structure Analysis by Particle Swarm Optimization (CALYPSO) algorithm [32, 33]. Its validity has been confirmed by successful predictions of a diverse variety of materials [34–37]. The detailed structural search procedure is described in the Supporting Information.

In this study, we performed the Vienna *ab initio* Simulation Package (VASP) based on density functional theory (DFT) to optimize structure and carry iterative calculation [38–40]. Within the framework of generalized gradient approximation (GGA), the exchange-correlation functional of Perdewe–Burkee–Ernzerh (PBE) [41, 42] was employed to relax the force of atom in the system. Until the energy difference is less than 10^{-5} eV and the force on each atom is small than 0.02 eV/Å between two electronic steps, all the optimization and self-consistent iteration will finish. The projected augmented wave (PAW) [43, 44] method and plane wave basis set with a cutoff energy of 400 eV are used. Brillouin zone of the PdSe monolayer is sampled in the MonkhorstPack scheme [45] with 3×5×1 k-point grids. A 20 Å vacuum distance is introduced to prevent negligible interlayer interactions. We performed phonon calculations as implemented in the PHONOPY program [46] to confirm the dynamical stability of the studied structures. The thermodynamic stability of the PdSe monolayer is verified by *ab initio* molecular dynamics (AIMD) simulations, and performed on a 3×3×1 supercell by using a canonical ensemble (NVT) with Nosé–Hoover method [47].

To investigate the thermodynamic stability of the Pd_xSe_y ($x = 2, 4$; $y = 2, 3, 4, 5, 6$) monolayer, the formation energies E_f of this structure were calculated by [4, 18, 48, 49]

$$E_f = E_{Pd_xSe_y} - [x \times (\mu_{Pd} + \Delta\mu_{Pd}) + y \times (\mu_{Se} + \Delta\mu_{Se})], \quad (1)$$

$$\Delta E_{Pd_2Se_4} = 2\Delta\mu_{Pd} + 4\Delta\mu_{Se}, \quad (2)$$

$$\Delta E_{Pd_2Se_4} = E_{Pd_2Se_4} - (2\mu_{Pd} + 4\mu_{Se}), \quad (3)$$

where $E_{Pd_xSe_y}$ is total energy of Pd_xSe_y monolayer. The x and y are the number of Pd and Se atoms in the structure, and the calculated chemical potentials μ_{Pd}(−5.22 eV) and μ_{Se}(−3.49 eV) are chosen from most stable phase of Pd and Se elements. respectively. The $\Delta\mu_{Pd}$ and $\Delta\mu_{Se}$ represent the variation of chemical potentials of Pd and Se atoms, and it can be tunable, but is restricted by Eq. (2). $\Delta E_{Pd_2Se_4}$ is the heat of formation of Pd_2Se_4 monolayer as defined in Eq. (3). One limit of $\Delta\mu_{Se}$ can be set to 0, where the system is at equilibrium with Se bulk (Se-rich), and the other limit is at equilibrium with Pd bulk (Pd-rich).

The formation enthalpy per atom ΔH is defined as [50]

$$\Delta H\,(Pd_xSe_y) = \frac{E_{Pd_xSe_y} - x \times \mu_{Pd} - y \times \mu_{Se}}{x + y}, \quad (4)$$

where the $\Delta H_{Pd_xSe_y}$ is the formation enthalpy per atom of Pd_xSe_y monolayer, respectively.

According to the deformation potential (DP) theory, the carrier mobility of PdSe monolayer can be expressed as [51–53]

$$\mu_{2D} = \frac{2eh^3C_{2D}}{3k_BT\,|m^*|^2\,E_1^2}, \quad (5)$$

where m^* and E_1 are the effective mass of the carrier and DP constant, respectively. m^* can be calculated by using the formula $m^* = h^2\left[\partial^2\varepsilon(k)/\partial k^2\right]^{-1}$. The elastic modulus C_{2D} in 2D system is given by $C_{2D} = \left(\partial^2E/\partial\delta^2\right)/S_0$, where E and S_0 define the total energy and the area of the optimized supercell, and δ is the applied uniaxial strain. k_B and T are Boltzmann's constant and temperature, respectively.

The optical absorption coefficient $I(\omega)$ can be expressed as [54–56]

$$I(\omega) = \sqrt{2}(\omega)\left[\sqrt{\varepsilon_1(\omega)^2 + \varepsilon_2(\omega)^2} - \varepsilon_1(\omega)\right]^{1/2}, \quad (6)$$

where $\varepsilon_1(\omega)$ is the real part of dielectric function which could be obtained from $\varepsilon_2(\omega)$ by Kramer–Kronig function.

3 Results and discussion

Although the bulk PdSe (space group $P4_2/m$) has been successfully synthesized, the PdSe monolayer remains experimentally and theoretically ambiguous. Recently, Lin

et al. reported that new Pd_4Se_6 monolayer can be produced by fusion of defective Pd_2Se_4 bilayers [30]. Stimulated by the synthesis process of Pd_4Se_6 monolayer, we artificially design several configurations with different stoichiometric ratios: Pd_2Se_2, Pd_2Se_3, Pd_4Se_4 and Pd_4Se_5 monolayers. As shown in Figs. 1(a)–(c), Pd_2Se_2 and Pd_2Se_3 structures are generated by removing two and one Se atoms of Pd_2Se_4 monolayers, respectively. Similarly, in Figs. 1(d)–(f), removing Se atoms from the Pd_4Se_6 monolayer can obtain Pd_4Se_4 and Pd_4Se_5 monolayers. Given the limitations of artificially designed structures, we further employ CALYPSO code to explore more new structures. By flexibly adjusting the input parameters in CALYPSO, such as space groups, chemical element ratio, lattice parameters, we can obtain more special allotropes.

Formation enthalpy is usually a metric of great importance to characterize the stability of structures. Thus, we summarize the formation enthalpies of the searched and designed structures in Fig. 2, and the formation enthalpies per-atom are calculated with respect to the stable phase of Pd and Se. As expected, the stable Pd_4Se_6 and Pd_2Se_4 form an obvious convex hull, where the point locating on or below the blank tie line corresponds to a thermodynamically stable phase. Fortunately, we finally predict a novel 2D PdSe monolayer by CALYPSO code and the detailed search procedure can be found in SI. Compared with other designed and searched structures, only PdSe locates closest to tie line with about 0.0067 eV/ atom deviation. This slight instability would be eliminated through the thermal affect at room temperature, then producing the stable

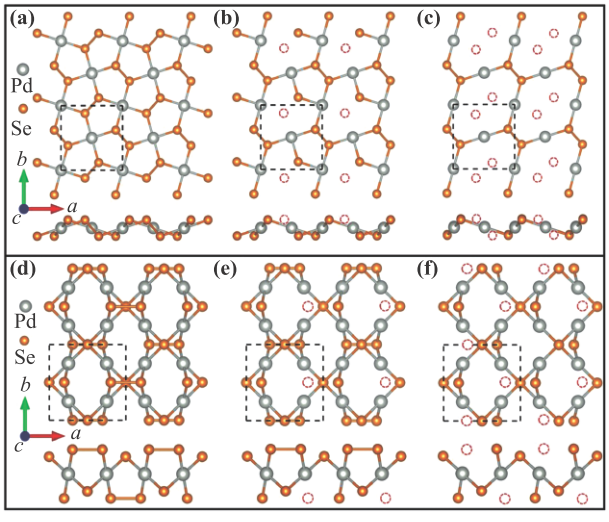

Fig. 1 Side and top view of the geometry structure of **(a)** Pd_2Se_4, **(b)** Pd_2Se_3, **(c)** Pd_2Se_2, **(d)** Pd_4Se_6, **(e)** Pd_4Se_5 and **(f)** Pd_4Se_4 monolayers. For better comparison, here we named after the number of atoms per unit cell. The orange and grey balls represent Pd and Se atoms, respectively. The dotted red circles denote the deleted atoms. The dashed rectangle marks primitive cell of monolayer.

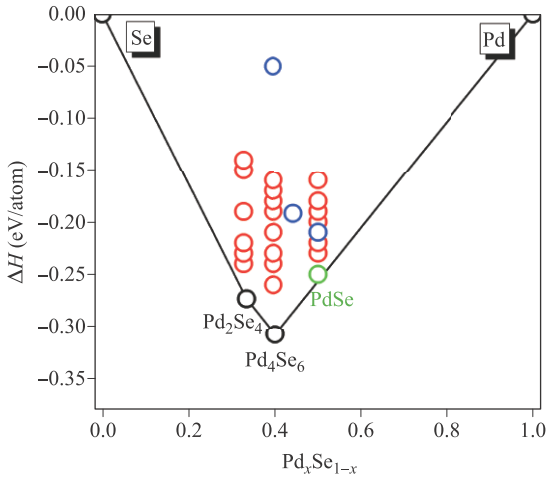

Fig. 2 Calculated convex hull diagram of $Pd_2Se_x(x = 2, 3, 4), Pd_4Se_y(y = 4, 5, 6)$ with respect to stable phase of Pd and Se, respectively. The black and blue circles represent Pd_2Se_4 (or Pd_4Se_6) and artificially designed structures, respectively. The red and green circles represent predicted structures by structural search based on the CALYPSO code.

PdSe phase. And this slight deviation may be caused by neglecting the influence of growth conditions (Pd-rich, Se-rich). In fact, the synthesis of the compounds is strongly dependent on the growth conditions.

Here in, we calculate corresponding formation energies (E_f) in Fig. 3(a) as a function of Se chemical potential, over the range of experimental environment from Pd-rich to Se-rich. For better comparison, we set the known Pd_2Se_4 monolayer as the reference phase. If formation energy line of one structure intersects with that of Pd_2Se_4 monolayer, indicating a stable phase. For example, the known stable Pd_4Se_6 monolayer has an obvious intersection with reference phase Pd_2Se_4 monolayer. However, we can clearly see that Pd_2Se_3 and Pd_4Se_5 monolayers

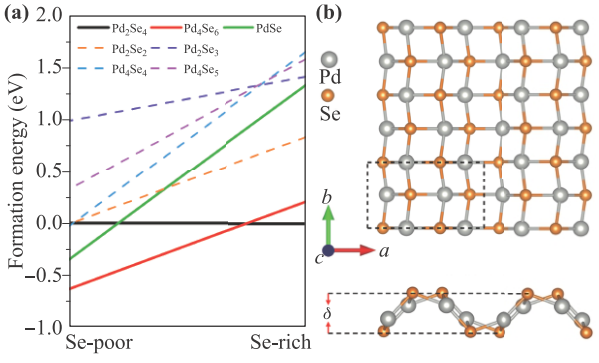

Fig. 3 **(a)** The E_f of the $Pd_2Se_x(x = 2-4)$ and $Pd_4Se_y(y = 4-6)$ monolayer as a function of μ_{Se}. The E_f of Pd_2Se_4 monolayer is shown by the black solid line as a reference. **(b)** Side and top view of PdSe monolayer. The gray and orange spheres represent Pd and Se atoms, respectively. The black dashed rectangle lines mark the unit cell.

are not stable within over whole chemical potential range. The E_f lines of Pd_2Se_2 and Pd_4Se_4 only intersect with the reference phase within a very small region under the ultimate Se-poor (Pd-rich) condition, which indicates that it is also difficult to generate these two phases in experiment. By extensive structure searching, we finally identify a novel stable PdSe monolayer in Fig. 3(b). As shown by green solid line, the E_f line of PdSe monolayer has intersected with that of Pd_2Se_4 monolayer and it possesses smaller E_f relative to the reference state in the vicinity of Se-poor, indicating that the PdSe monolayer can be favorably stable by tuning the growth conditions. As shown in Fig. 3(b), PdSe monolayer displays P21/m symmetry (point group C_{2h}) with a tetragonal lattice and the optimized lattice constants $a = 8.07$ Å and $b = 4.67$ Å. Per unit cell contains four Pd and four Se atoms, and each Pd (Se) atom is bonded to four Se (Pd) atoms in the different atom layer. In our calculation, the longest and shortest Pd–Se bond lengths are 2.51 Å and 2.48 Å, respectively, almost the same as the Pd_2Se_4 and Pd_4Se_6 monolayers. In PdSe monolayer, there only exists Pd–Se bond, but Pd_4Se_6 and Pd_2Se_4 monolayers possess both Pd–Se and Se–Se bonds. Interesting, from the side view, this structure exhibits puckered camelback character with a vertical puckering distance of 2.67 Å, in which Se and Pd atoms locate the outermost and middle atom layers, respectively. In addition, Pd atoms in these monolayers all bond with surrounding 4 Se atoms with coordination numbers (N_c) of 4. However, there is obvious difference for the N_c of Se. For example, Se atoms of Pd_2Se_4 and PdSe only have single coordination numbers of $N_c = 3$ and 4, respectively.

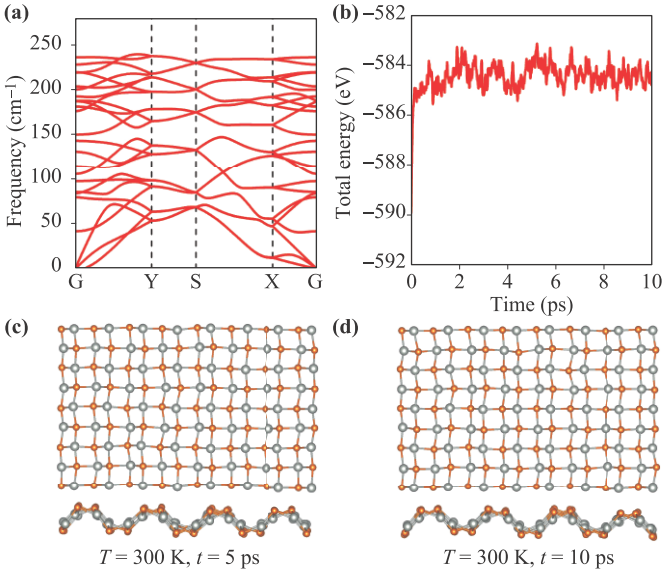

Fig. 4 **(a)** Phonon dispersion of PdSe monolayer along the high-symmetry points. **(b)** Fluctuation of total energy during the MD simulations for PdSe monolayer, **(c)** and **(d)** Snapshots of *ab initio* MD simulations for PdSe monolayer at $T = 300$ K and different annealing time of 5 and 10 ps.

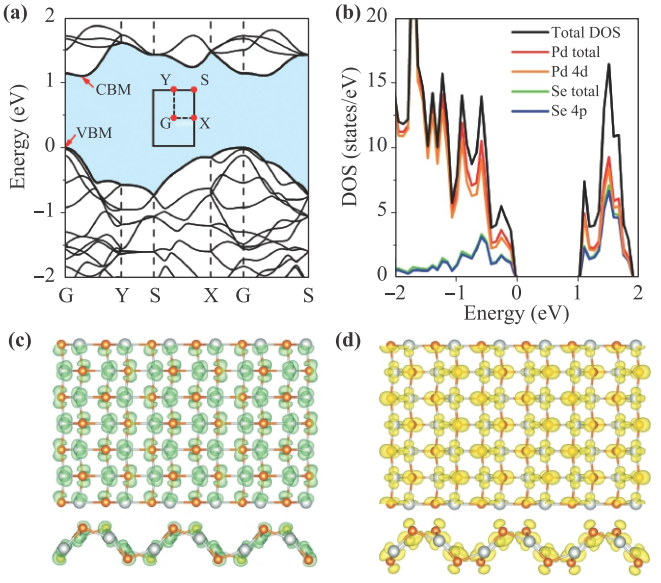

Fig. 5 **(a)** Electronic band structure of PdSe monolayer. Inset in (a) shows the Brillouin zone of PdSe 2D crystals with high symmetry points labeled. The Fermi level is assigned at 0 eV. **(b)** The density of states (DOS) of PdSe monolayer. **(c, d)** Spatial distribution of electron density in VBM and CBM (0.0005 e/Å^3).

Pd_4Se_6 possesses two distinct types of Se atoms with both $N_c = 3$ and 4. Considering that Se dimmer bonding exists only in Pd_2Se_4 and Pd_4Se_6, not in PdSe monolayer, so the multiple valence state of Pd and Se ions plays a key role in stabilizing the PdSe monolayer structure.

In order to further verify the structural stability of PdSe monolayer, we perform the phonon-dispersion calculation as shown in Fig. 4(a). Obviously, there is no imaginary-frequency phonon mode in the first Brillouin zone, indicating that our predicted PdSe monolayer is thermodynamically stable. As shown in Fig. 4(b), we also examine the dynamic stability using *ab initio* molecular dynamic (AIMD) simulations at room temperature of 300 K. Figures 4(c) and (d) show the snapshots of PdSe monolayer at 300 K up to a time period of 5 ps and 10 ps, respectively. Compared with snapshot at 0 ps, from top and side views, the free-standing PdSe monolayer hardly changes, revealing the high structural rigidity. Above all of calculations about stability indicate that there is a great possibility to synthesize PdSe monolayer by appropriate methods.

Figure 5(a) shows the band structure of PdSe monolayer obtained within the PBE scheme. The PBE and Heyd–Scuseria–Ernzerhof (HSE06) hybrid functional [57] are two common functionals for studying band structures of semiconductors. As is well known that HSE06 functional can predict many semiconductor band gaps more accurately, but it will overestimate the band gap of some TMDs material [58–60]. Considering that the band gap of Pd_2Se_4 has been experimentally measured [61], thus we select Pd_2Se_4 bulk to test the accuracy of function-

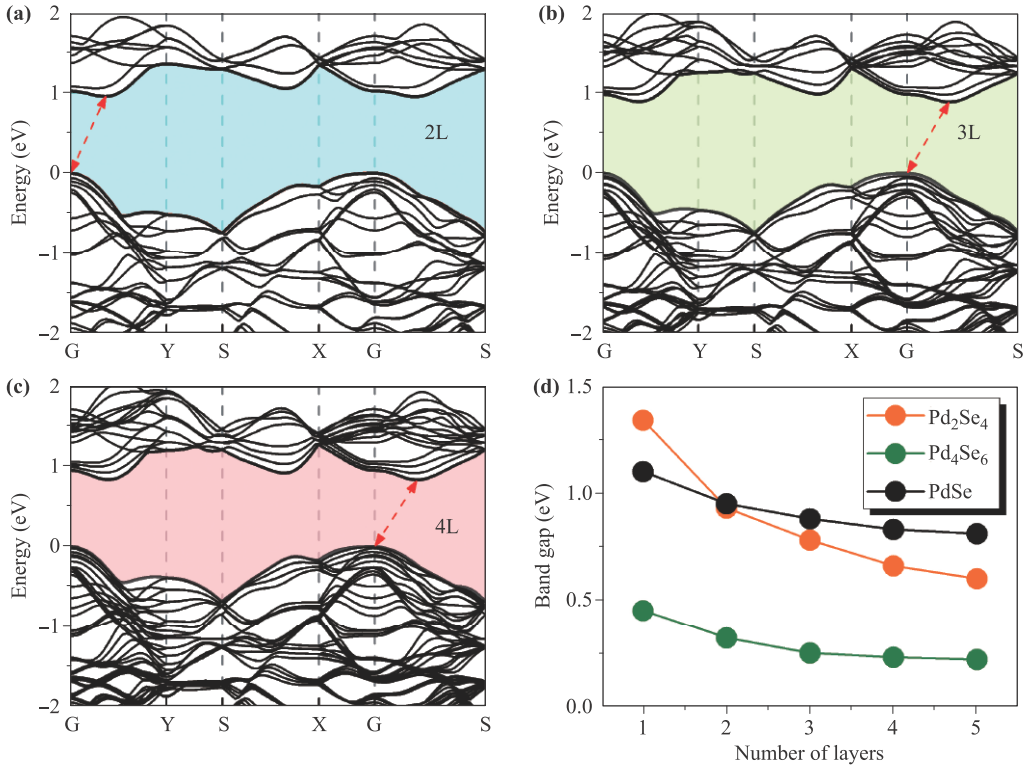

Fig. 6 Calculated electronic band structure of **(a)** 2 L, **(b)** 3 L and **(c)** 4 L PdSe layers. **(d)** Variation of bandgap of PdSe, Pd_2Se_4 and Pd_4Se_6 as a function of number of layers. The black, orange and olive solid lines represent PdSe, Pd_2Se_4 and Pd_4Se_6 layers, respectively.

als. As shown in Fig. S1 (Supplementary information), the band gap of Pd_2Se_4 bulk calculated by PBE and HSE06 schemes are 0.39 eV and 1.20 eV, respectively. And for Pd_2Se_4 monolayer, the PBE (1.33 eV) and HSE06 (1.34 eV) schemes show similar band structure results. Comparing the bandgap of experiment (0 eV for bulk and 1.28 eV for monolayer) and calculated results, the PBE functional was more suitable to calculate the electronic properties of the Pd–Se system. In Fig. 5(a), it was clearly shown that PdSe monolayer exhibits indirect semiconductor property with band gap of 1.10 eV. The valence band maximum (VBM) located on the $G(0, 0, 0)$ point, while the conduction band minimum (CBM) located between the high-symmetry G and $Y(0, 0.5, 0)$ points. Figure 5(b) presents the total and partial density of states (DOS) of PdSe monolayer. Analysis of the curve reveals that the electronic states of valence band edge and conduction band edge are primarily dominated by the d-states of Pd atoms and p-states of Se atoms. Because of the covalent bonding of Se–Pd at the inferior atomic planes, it leads to the hybridization between the Pd4d and Se4p states. These orbital features are similar to the Pd_2Se_4 monolayer, but are different from Pd_4Se_6 monolayer, in which VBM mainly origins from the d-states of Pd atoms, as shown in Fig. S2(f) (Supplementary information). For further gaining insights into the electronic properties, the spatial charge distributions of the VBM and CBM of PdSe monolayer are also displayed in Figs. 5(c) and (d), which exhibit similar orbital features as DOS. In addition, we also consider the influence of spin orbital coupling (SOC) interaction in band structure of PdSe monolayer. As shown in Fig. S3 (Supplementary information), the SOC has a weak influence on the band structure of PdSe monolayer, in which the band gap, valence and conduction band edge keep almost unchanged. Therefore, we will not consider the SOC interaction in the following study.

The magnitude of carrier (electron and hole) mobility is crucial for the performance of electronic devices. To this end, on the basis of calculated band structure, we next focus on evaluating the carrier transport property of PdSe monolayer within effective mass approximation and deformation potential theory. According to this theory, the deformation potential constant E_1 and elastic modulus C_{2D} was be derived, as shown in Fig. S4 (Supplementary information). The resulting effective mass (m^*), 2D in-plane stiffness (C_{2D}), deformation-potential constant (E_1) and carrier mobility (μ) are summarized in Table 1. Obviously, the electron and hole effective masses of PdSe monolayer show highly anisotropic characteristic along different directions of the unit cell, which is consistent with the asymmetric frontierconduction and valance band structures in Fig. 5(a). And the in-plane stiff-

Table 1 Calculated deformation-potential constant (E_1), 2D in-plane stiffness (C_{2D}), effective mass (m^*) and carrier mobility (μ) along the $x(a)$ and $y(b)$ directions for a PdSe monolayer at 300 K.

Carriers type	m^* (m_e)	C_{2D} (eV/A^2)	E_1 (eV)	μ (cm$^2\cdot$V$^{-1}\cdot$s^{-1})
Electron (x)	18.79	4.56	−0.2	22.07
Electron (y)	1.15	4.56	−1.45	4.35
Hole (x)	−6.63	7.43	−5.07	2398.80
Hole (y)	−0.83	7.43	−6.39	1.61

ness and deformation-potential constant also exhibit obvious direction-dependent anisotropy, which mainly origins from the different arrangement of Pd and Se atoms along x and y directions. For carrier mobility, the anisotropic property of electron is not pronounced. However, hole mobility shows great anisotropy and the highest hole mobility of PdSe monolayer along the x direction is predicted to be 2398.8 cm$^2\cdot$V$^{-1}\cdot$s^{-1}, which is much larger than that of Pd_4Se_6 monolayer (84.92 cm$^2\cdot$V$^{-1}\cdot$s^{-1}) and is quite close to that of Pd_2Se_4 monolayer (1928.99 cm$^2\cdot$V$^{-1}\cdot$s^{-1}). Remarkably, in both x and y directions, PdSe monolayer exhibits higher hole mobility than electron, which indicates that the carrier transport of PdSe monolayer is dominated by hole.

As we all know that the electronic band property of TMDs (such as MoS_2) exhibits strongly thickness-dependence effect [62, 63]. In Fig. 6, we also discuss the influence of thickness effect on the band structure of PdSe layers. It clearly shows that with the increase of the layer thickness, PdSe system exhibits obvious quantum confinement effect. The band gap gradually decreases from 0.95 eV for bilayer to 0.88 eV for trilayer and 0.83 eV for four-layers as shown in Figs. 6(a)–(c), but still keeps the indirect semiconductor property. In Fig. S5 (Supplementary information), we also display the electronic band structures of monolayer, bilayer and trilayer of Pd_2Se_4 and Pd_4Se_6. Similarly, Pd_2Se_4 and Pd_4Se_6 also exhibit decreased band gap due to the thickness effect. Moreover, we investigate the sensitivity of the band gap to the thickness effect of different Pd–Se system. As shown in Fig. 6(d), as the layer number increases, the band gaps of PdSe and Pd_4Se_6 exhibit almost same sensitivity with a similar decreasing trend of first steepening then flattening, which indicates that the quantum confinement effect gradually weakens with the increase of layer thickness. However, the Pd_2Se_4 possesses the strong sensitivity to the number of layers. Comparing to PdSe and Pd_4Se_6, the band gaps of Pd_2Se_4 show a steeper decreasing trend from 1 L to 4 L.

According to the calculated electronic band gap, PdSe monolayer is expected to possess excellent performance for optical absorption. Figure 7 shows the calculated optical absorption spectrum of PdSe monolayer along x- and y-directions to characterize its optical properties. The adsorption coefficients of Pd_2Se_4 and Pd_4Se_6 monolayers are also included for comparison. It is clearly shown that the optical properties of PdSe monolayer exhibit obviously anisotropic feature due to the intrinsic structure anisotropy. Along the y-direction, PdSe monolayer possesses high absorption coefficients in both visible and ultraviolet regions. In the x-direction, absorption coefficients show a reduction, especially in the ultraviolet region. But the absorption coefficients of PdSe monolayer are with the order of 10^5 cm^{-1} in both x- and y-directions that are considerably desirable for optical absorption. Similarly, Pd_2Se_4 and Pd_4Se_6 monolayers also show anisotropic absorption coefficients along x- and y-directions. By comparison, we can find that in the visible region, Pd_2Se_4 and Pd_4Se_6 monolayers have lower optic absorption coefficients relative to PdSe monolayer along both x- and y-directions. For the ultraviolet region, y-direction of PdSe monolayer still possesses higher absorption coefficients than Pd_2Se_4 and Pd_4Se_6 monolayer. The broad absorption region and large absorption coefficient render the PdSe monolayer as a potential candidate for photovoltaics and optoelectronic devise.

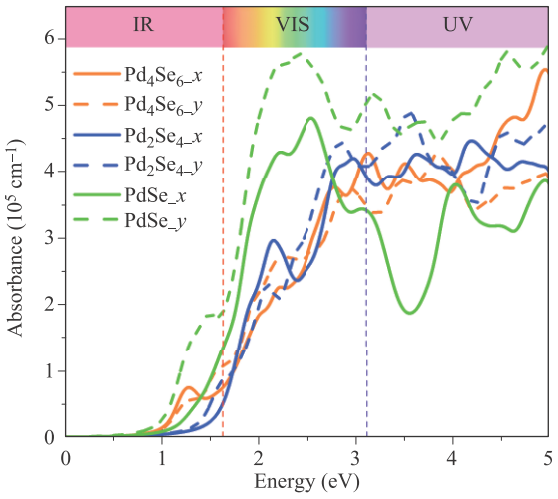

Fig. 7 The calculated optical absorption spectra of PdSe, Pd_2Se_4 and Pd_4Se_6 monolayers. IR, VIS and UV are the abbreviations of infrared, visible and ultraviolet regions, respectively.

4 Conclusions

In summary, we have predicted a hitherto unknown semiconducting PdSe monolayer by CALYPSO code. Based on comprehensive DFT computations, we systematically studied the structure, stability, electronic and optical properties of PdSe monolayer. The calculated results show that the PdSe monolayer possesses a puckered tetragonal lattice with good dynamics and thermodynamic stabilities. The electronic structure calculations indicate that PdSe monolayer exhibits indirect semiconducting charac-

teristic with a desirable band gap of 1.1 eV for optical absorption. The structure anisotropy endows the PdSe with remarkable anisotropic carrier mobility and the transport behavior is mainly dominated by the hole carrier. The optical properties also show anisotropic feature with large absorption coefficient within a broad absorption region. We believe that this study will promote the experimental synthesis of this new 2D PdSe structure and further studies about their application in optoelectronic devices in the future.

Electronic supplementary materials are available in the online version of this article at https://doi.org/10.1007/s11467-022-1154-5 and http://journal.hep. com.cn/fop/EN/10.1007/s11467-022-1154-5 and are accessible for authorized users.

Acknowledgements This work was supported by the National Natural Science Foundation of China with Grant Nos. 11604092, 11634001, 12104385 and the National Basic Research Programs of China under Grant No. 2016YFA0300900. The computational resources were provided by the computation platform of National Super-Computer Center in Changsha, China.

References

1. H. Li, Q. Zhang, C. C. R. Yap, B. K. Tay, T. H. T. Edwin, A. Olivier, and D. Baillargeat, From bulk to monolayer MoS_2: Evolution of Raman scattering, *Adv. Funct. Mater.* 22(7), 1385 (2012)
2. J. Sun, H. Shi, T. Siegrist, and D. J. Singh, Electronic, transport, and optical properties of bulk and mono-layer $PdSe_2$, *Appl. Phys. Lett.* 107(15), 153902 (2015)
3. X. X. Xue, S. Shen, X. Jiang, P. Sengdala, K. Chen, and Y. Feng, Tuning the catalytic property of phosphorene for oxygen evolution and reduction reactions by changing oxidation degree, *J. Phys. Chem. Lett.* 10(12), 3440 (2019)
4. X. X. Xue, L. M. Tang, K. Chen, L. Zhang, E. G. Wang, and Y. Feng, Bifunctional mechanism of N, P co-doped graphene for catalyzing oxygen reduction and evolution reactions, *J. Chem. Phys.* 150(10), 104701 (2019)
5. M. Qiao, J. Liu, Y. Wang, Y. Li, and Z. Chen, $PdSeO_3$ monolayer: Promising inorganic 2D photocatalyst for direct overall water splitting without using sacrificial reagents and cocatalysts, *J. Am. Chem. Soc.* 140(38), 12256 (2018)
6. K. S. Novoselov, V. I. Fal ko, L. Colombo, P. R. Gellert, M. G. Schwab, and K. Kim, A roadmap for graphene, *Nature* 490(7419), 192 (2012)
7. K. S. Novoselov, A. K. Geim, S. V. Morozov, D. Jiang, Y. Zhang, S. V. Dubonos, I. V. Grigorieva, and A. A. Firsov, Electric field effect in atomically thin carbon films, *Science* 306(5696), 666 (2004)
8. K. S. Novoselov, D. V. Andreeva, W. C. Ren, and G. C. Shan, Graphene and other two-dimensional materials, *Front. Phys.* 14(1), 13301 (2019)
9. X. Lu, P. Stepanov, W. Yang, M. Xie, M. A. Aamir, I. Das, C. Urgell, K. Watanabe, T. Taniguchi, G. Zhang, A. Bachtold, A. H. MacDonald, and D. K. Efetov, Superconductors, orbital magnets and correlated states in magic-angle bilayer graphene, *Nature* 574(7780), 653 (2019)
10. M. Yankowitz, S. Chen, H. Polshyn, Y. Zhang, K. Watanabe, T. Taniguchi, D. Graf, A. F. Young, and C. R. Dean, Tuning superconductivity in twisted bilayer graphene, *Science* 363(6431), 1059 (2019)
11. Y. Cao, V. Fatemi, S. Fang, K. Watanabe, T. Taniguchi, E. Kaxiras, and P. Jarillo-Herrero, Unconventional superconductivity in magic-angle graphene superlattices, *Nature* 556(7699), 43 (2018)
12. Y. Cao, V. Fatemi, A. Demir, S. Fang, S. L. Tomarken, J. Y. Luo, J. D. Sanchez-Yamagishi, K. Watanabe, T. Taniguchi, E. Kaxiras, R. C. Ashoori, and P. Jarillo-Herrero, Correlated insulator behaviour at half-filling in magic-angle graphene superlattices, *Nature* 556(7699), 80 (2018)
13. C. Zhi, Y. Bando, C. Tang, H. Kuwahara, and D. Golberg, Large-scale fabrication of boron nitride nanosheets and their utilization in polymeric composites with improved thermal and mechanical properties, *Adv. Mater.* 21(28), 2889 (2009)
14. J. H. Warner, M. H. Rummeli, A. Bachmatiuk, and B. Buchner, Atomic resolution imaging and topography of boron nitride sheets produced by chemical exfoliation, *ACS Nano* 4(3), 1299 (2010)
15. R. J. Smith, P. J. King, M. Lotya, C. Wirtz, U. Khan, S. De, A. O'Neill, G. S. Duesberg, J. C. Grunlan, G. Moriarty, J. Chen, J. Wang, A. I. Minett, V. Nicolosi, and J. N. Coleman, Large-scale exfoliation of inorganic layered compounds in aqueous surfactant solutions, *Adv. Mater.* 23(34), 3944 (2011)
16. J. Mao, Y. Wang, Z. Zheng, and D. Deng, The rise of two-dimensional MoS_2 for catalysis, *Front. Phys.* 13(4), 138118 (2018)
17. Y. Liu, Y. Zhou, H. Zhang, F. Ran, W. Zhao, L. Wang, C. Pei, J. Zhang, X. Huang, and H. Li, Probing interlayer interactions in WSe_2-graphene heterostructures by ultralow-frequency Raman spectroscopy, *Front. Phys.* 14(1), 13607 (2019)
18. X. X. Xue, Y. Feng, K. Chen, and L. Zhang, The vertical growth of MoS_2 layers at the initial stage of CVD from first-principles, *J. Chem. Phys.* 148(13), 134704 (2018)
19. J. Qiao, X. Kong, Z. X. Hu, F. Yang, and W. Ji, High-mobility transport anisotropy and linear dichroism in few-layer black phosphorus, *Nat. Commun.* 5(1), 4475 (2014)
20. H. Liu, A. T. Neal, Z. Zhu, Z. Luo, X. Xu, D. Tomanek, and P. D. Ye, Phosphorene: An unexplored 2D semiconductor with a high hole mobility, *ACS Nano* 8(4), 4033 (2014)
21. L. Li, Y. Yu, G. J. Ye, Q. Ge, X. Ou, H. Wu, D. Feng, X. H. Chen, and Y. Zhang, Black phosphorus field-effect transistors, *Nat. Nanotechnol.* 9(5), 372 (2014)

22. L. P. Tang, L. M. Tang, H. Geng, Y. P. Yi, Z. Wei, K. Q. Chen, and H. X. Deng, Tuning transport performance in two-dimensional metal-organic framework semiconductors: Role of the metal *d* band, *Appl. Phys. Lett.* 112(1), 012101 (2018)
23. S. L. James, Metal–organic frameworks, *Chem. Soc. Rev.* 32(5), 276 (2003)
24. L. Sun, M. G. Campbell, and M. Dinca, Electrically conductive porous metal-organic frameworks, *Angew. Chem. Int. Ed.* 55(11), 3566 (2016)
25. A. J. Mannix, X. F. Zhou, B. Kiraly, J. D. Wood, D. Alducin, B. D. Myers, X. Liu, B. L. Fisher, U. Santiago, J. R. Guest, M. J. Yacaman, A. Ponce, A. R. Oganov, M. C. Hersam, and N. P. Guisinger, Synthesis of borophenes: Anisotropic, two-dimensional boron polymorphs, *Science* 350(6267), 1513 (2015)
26. Z. Zhang, Y. Yang, E. S. Penev, and B. I. Yakobson, Elasticity, flexibility, and ideal strength of borophenes, *Adv. Funct. Mater.* 27(9), 1605059 (2017)
27. B. K. Agrawal, P. S. Yadav, S. Kumar, and S. Agrawal, First-principles calculation of Ga-based semiconductors, *Phys. Rev. B* 52(7), 4896 (1995)
28. S. Massidda, A. Continenza, A. J. Freeman, T. M. de Pascale, F. Meloni, and M. Serra, Structural and electronic properties of narrow-band-gap semiconductors: InP, InAs, and InSb, *Phys. Rev. B* 41(17), 12079 (1990)
29. G. D. Nguyen, L. Liang, Q. Zou, M. Fu, A. D. Oyedele, B. G. Sumpter, Z. Liu, Z. Gai, K. Xiao, and A. P. Li, 3D imaging and manipulation of subsurface selenium vacancies in $PdSe_2$, *Phys. Rev. Lett.* 121(8), 086101 (2018)
30. J. Lin, S. Zuluaga, P. Yu, Z. Liu, S. T. Pantelides, and K. Suenaga, Novel Pd_2Se_3 two-dimensional phase driven by interlayer fusion in layered $PdSe_2$, *Phys. Rev. Lett.* 119(1), 016101 (2017)
31. X. Zhu, F. Li, Y. Wang, M. Qiao, and Y. Li, Pd_2Se_3 monolayer: A novel two-dimensional material with excellent electronic, transport, and optical properties, *J. Mater. Chem. C* 6(16), 4494 (2018)
32. Y. Wang, J. Lv, L. Zhu, and Y. Ma, Crystal structure prediction via particle-swarm optimization, *Phys. Rev. B* 82(9), 094116 (2010)
33. Y. Wang, J. Lv, L. Zhu, and Y. Ma, CALYPSO: A method for crystal structure prediction, *J. Mater. Chem. C* 183(10), 2063 (2012)
34. Y. Wang, M. Miao, J. Lv, L. Zhu, K. Yin, H. Liu, and Y. Ma, An effective structure prediction method for layered materials based on 2D particle swarm optimization algorithm, *J. Chem. Phys.* 137(22), 224108 (2012)
35. J. Lv, Y. Wang, L. Zhu, and Y. Ma, Particle-swarm structure prediction on clusters, *J. Chem. Phys.* 137(8), 084104 (2012)
36. X. Jiang, Y. Zheng, X. X. Xue, J. Dai, and Y. Feng, *Ab initio* study of the miscibility for solid hydrogen-helium mixtures at high pressure, *J. Chem. Phys.* 152(7), 074701 (2020)
37. K. Hu, J. Lian, L. Zhu, Q. Chen, and S. Y. Xie, Prediction of Fe_2P-type $TiTe_2$ under pressure, *Phys. Rev. B* 101(13), 134109 (2020)
38. G. Kresse and J. Furthmuller, Efficient iterative schemes for *ab initio* total-energy calculations using a plane-wave basis set, *Phys. Rev. B* 54(16), 11169 (1996)
39. G. Kresse and J. Hafner, *Ab initio* molecular dynamics for liquid metals, *Phys. Rev. B* 47(1), 558 (1993)
40. G. Kresse, J. Furthmuller, and J. Hafner, Theory of the crystal structures of selenium and tellurium: The effect of generalized-gradient corrections to the local-density approximation, *Phys. Rev. B* 50(18), 13181 (1994)
41. J. P. Perdew, K. Burke, and M. Ernzerhof, Generalized gradient approximation made simple, *Phys. Rev. Lett.* 77(18), 3865 (1996)
42. Y. Zheng, X. Jiang, X. Xue, J. Dai, and Y. Feng, *Ab initio* study of pressure-driven phase transition in $FePS_3$ and $FePSe_3$, *Phys. Rev. B* 100(17), 174102 (2019)
43. G. Kresse and D. Joubert, From ultrasoft pseudopotentials to the projector augmente *d*-wave method, *Phys. Rev. B* 59(3), 1758 (1999)
44. P. E. Blöchl, Projector augmente *d*-wave method, *Phys. Rev. B* 50(24), 17953 (1994)
45. H. J. Monkhorst and J. D. Pack, Special points for Brillouin-zone integrations, *Phys. Rev. B* 13(12), 5188 (1976)
46. A. Togo, F. Oba, and I. Tanaka, First-principles calculations of the ferroelastic transition between rutile-type and $CaCl_2$-type SiO_2 at high pressures, *Phys. Rev. B* 78(13), 134106 (2008)
47. G. J. Martyna, M. L. Klein, and M. Tuckerman, Nosé–Hoover chains: The canonical ensemble via continuous dynamics, *J. Chem. Phys.* 97(4), 2635 (1992)
48. Y. Feng, F. Li, Z. Hu, X. Luo, L. Zhang, X. F. Zhou, H. T. Wang, J. J. Xu, and E. G. Wang, Tuning the catalytic property of nitrogen-doped graphene for cathode oxygen reduction reaction, *Phys. Rev. B* 85(15), 155454 (2012)
49. W. Zhou, X. Zou, S. Najmaei, Z. Liu, Y. Shi, J. Kong, J. Lou, P. M. Ajayan, B. I. Yakobson, and J. C. Idrobo, Intrinsic structural defects in monolayer molybdenum disulfide, *Nano Lett.* 13(6), 2615 (2013)
50. Y. Feng, K. Chen, X. Z. Li, E. Wang, and L. Zhang, Hydrogen induced contrasting modes of initial nucleations of graphene on transition metal surfaces, *J. Chem. Phys.* 146(3), 034704 (2017)
51. J. Tan, K. Chen, and L. M. Tang, Out-of-plane spontaneous polarization and superior photoelectricity in two-dimensional SiSn, *J. Phys.: Condens. Matter* 32(6), 065003 (2020)
52. J. Bardeen and W. Shockley, Deformation potentials and mobilities in non-polar crystals, *Phys. Rev.* 80(1), 72 (1950)
53. A. Franceschetti, S. H. Wei, and A. Zunger, Effects of ordering on the electron effective mass and strain deformation potential in $GaInP_2$: Deficiencies of the $\boldsymbol{k.p}$ model, *Phys. Rev. B* 52(19), 13992 (1995)
54. S. Saha, T. P. Sinha, and A. Mookerjee, Electronic structure, chemical bonding, and optical properties of paraelectric $BaTiO_3$, *Phys. Rev. B* 62(13), 8828 (2000)

55. N. Miao, B. Xu, N. C. Bristowe, J. Zhou, and Z. Sun, Tunable magnetism and extraordinary sunlight absorbance in indium triphosphide monolayer, *J. Am. Chem. Soc.* 139(32), 11125 (2017)
56. Y. F. Ding, Q. Q. Zhao, Z. L. Yu, Y. Q. Zhao, B. Liu, P. B. He, H. Zhou, K. Li, S. F. Yin, and M. Q. Cai, Strong thickness-dependent quantum confinement in all-inorganic perovskite Cs_2PbI_4 with a Ruddlesden–Popper structure, *J. Mater. Chem. C* 7(24), 7433 (2019)
57. A. D. Becke, Perspective: Fifty years of density-functional theory in chemical physics, *J. Chem. Phys.* 140(18), 18A301 (2014)
58. K. F. Mak, C. Lee, J. Hone, J. Shan, and T. F. Heinz, Atomically thin MoS_2: A new direct-gap semiconductor, *Phys. Rev. Lett.* 105(13), 136805 (2010)
59. S. Lebègue and O. Eriksson, Electronic structure of two-dimensional crystals from *ab initio* theory, *Phys. Rev. B* 79(11), 115409 (2009)
60. C. Ataca and S. Ciraci, Functionalization of single-layer MoS_2 honeycomb structures, *J. Mater. Chem. C* 115(27), 13303 (2011)
61. A. D. Oyedele, S. Yang, L. Liang, A. A. Puretzky, K. Wang, J. Zhang, P. Yu, P. R. Pudasaini, A. W. Ghosh, Z. Liu, C. M. Rouleau, B. G. Sumpter, M. F. Chisholm, W. Zhou, P. D. Rack, D. B. Geohegan, and K. Xiao, $PdSe_2$: Pentagonal two-dimensional layers with high air stability for electronics, *J. Am. Chem. Soc.* 139(40), 14090 (2017)
62. B. Chakraborty, H. S. S. R. Matte, A. K. Sood, and C. N. R. Rao, Layer-dependent resonant Raman scattering of a few layer MoS_2, *J. Raman Spectrosc.* 44(1), 92 (2013)
63. W. Jin, P. C. Yeh, N. Zaki, D. Zhang, J. T. Sadowski, A. Al-Mahboob, A. M. van der Zande, D. A. Chenet, J. I. Dadap, I. P. Herman, P. Sutter, J. Hone, and Osgood, Direct measurement of the thickness-dependent electronic band structure of MoS_2 using angle-resolved photoemission spectroscopy, *Phys. Rev. Lett.* 111(10), 106801 (2013)